This is the accepted manuscript made available via CHORUS. The article has been published as:

Optical properties of highly compressed polystyrene: An ab initio study

S. X. Hu (□□□), L. A. Collins, J. P. Colgan, V. N. Goncharov, and D. P. Kilcrease

Phys. Rev. B **96**, 144203 — Published 16 October 2017

DOI: 10.1103/PhysRevB.96.144203

Optical Properties of Highly Compressed Polystyrene (CH): An *ab initio* Study

S. X. Hu (胡素兴)[1,*], L. A. Collins[2], J. P. Colgan[2], V. N. Goncharov[1], D. P. Kilcrease[2]

[1]Laboratory for Laser Energetics, University of Rochester,

250 E. River Road, Rochester, NY 14623

[2]Theoretical Division, Los Alamos National Laboratory, Los Alamos, NM 87545

E-mail: shu@lle.rochester.edu

Using all-electron density functional theory, we have performed an *ab initio* study on x-ray absorption spectra of highly compressed polystyrene (CH). We found that the K-edge shifts in strongly coupled, degenerate polystyrene cannot be explained by existing continuum-lowering models adopted in traditional plasma physics. To gain insights into the K-edge shift in warm, dense CH, we have developed a model designated as "single-mixture-in-a-box" (*SMIAB*), which incorporates both the lowering of continuum and the rising of Fermi surface resulting from high compression. This simple *SMIAB* model correctly predicts the K-edge shift of carbon in highly compressed CH in good agreement with results from quantum-molecular-dynamics (QMD) calculations. Traditional opacity models failed to give the proper K-edge shifts as the CH density increased. Based on QMD calculations, we have established a first-principles opacity table (FPOT) for CH in a wide range of densities and temperatures [ρ = 0.1 to 100 g/cm^3 and T = 2000 to 1,000,000 K]. The FPOT gives much higher Rosseland mean opacity compared to the cold-opacity–patched astrophysics opacity table for warm, dense CH and favorably compares to the newly improved Los Alamos *ATOMIC* model for moderately compressed CH ($\rho_{CH} \leq$

10 g/cm^3) but remains a factor of 2 to 3 higher at extremely high densities ($\rho_{CH} \geq 50$ g/cm^3). We anticipate the established FPOT of CH will find important applications to reliable designs of high-energy-density experiments. Moreover, the understanding of K-edge shifting revealed in this study could provide guides for improving the traditional opacity models to properly handle the strongly coupled and degenerate conditions.

PACS numbers 52.25.Os, 52.27.Gr, 78.20.Ci

I. INTRODUCTION

Optical properties characterize the response of materials to external electromagnetic radiation ranging from microwaves to x rays. For materials at ambient conditions, optical spectroscopic probes often reveal the intricacies of the electronic structure. Heating and compression can cause variations in the spectroscopic features, reflecting the changing environment experienced by the atoms in the material.[1–6] In turn, such spectroscopic measurements can be used to accurately infer information about the electron density and temperature in materials under extreme conditions, provided that reliable theoretical models can be applied. Traditional *ATOMIC* models[7–11] exist for plasma spectroscopy under classical plasma conditions. These models are employed to incorporate density and temperature effects, including line broadening and shifting, into the calculations of plasma spectroscopy[12–14] by atomic physics codes and generally provide a reliable guide to understanding the spectral features in diluted and hot plasma conditions. These traditional models can break down, however, for dense plasmas. For example, recent experimental studies[15–19] have revealed a lack of understanding of line shifting in hot but dense plasmas and have stimulated renewed

theoretical interest[20–23] to the important physical concept of *continuum lowering or ionization potential depression* (*IPD*). So far, these studies have been limited to a strongly coupled but nondegenerate plasma regime (i.e., solid density or moderately compressed hot plasma conditions). How atomic physics can be modified further for extremely compressed materials at relatively low temperatures remains to be answered. Namely, the optical properties of strongly coupled, fully degenerate materials under high compression might be completely different from our understandings gained from existing studies.

Matter at extreme conditions of density and temperature exists in many natural environments such as in astrophysical objects like brown dwarfs and planetary interiors. Recently, various high-energy-density (HED) facilities have achieved such exotic material conditions. For example, the imploding shell of an inertial confinement fusion (ICF) target[24–28] can reach compressions of hundreds or even thousands times ambient conditions with its temperature still remaining below its Fermi temperature.[29,30] In such HED systems, the optical properties (opacity/emissivity) determine the radiation energy transport. Therefore, a theoretical understanding of the optical properties of extremely dense and warm matter becomes essential in order to complement the experimental campaigns. This endeavor will not only provide reliable opacity/emissivity tables for ICF/HED experimental designs but will also make it possible to examine extreme HED systems using traditional spectroscopic tools.

Polystyrene (CH) is one of the materials often chosen for high-energy-density–physics (HEDP) and ICF target designs. Its optical properties, such as x-ray absorption under extreme conditions, are crucial for understanding the response of dense material mixtures to electromagnetic radiations. In this paper, we present a comprehensive *ab initio* study of the opacity of polystyrene over a wide range of densities and temperatures. Using the quantum

molecular dynamics (QMD) method, based on an all-electron density-functional theory (DFT), we thoroughly investigated the behavior of x-ray absorption in response to changes in various conditions. Our *ab initio* results revealed certain mechanisms behind the shift in the carbon K edge in very dense polystyrene that cannot be explained by existing continuum-lowering models. Instead, the behavior of the K-edge shift can only be understood through combining the lowering of the continuum and the rising of the Fermi surface. Performing such *ab initio* calculations over the various densities (ρ_{CH} = 0.1 to 100 g/cm^3) and temperatures (T = 2000 to 1,000,000 K), we produced a first-principles opacity table (FPOT) of CH for ICF/HEDP applications. We find that our QMD-based FPOT gives an-order-of-magnitude higher opacity than the widely used astrophysics opacity table (AOT)[31] for soft x rays below the carbon K edge. On the other hand, comparisons with modern opacity libraries such as the newly revised *ATOMIC* model[32] agree favorably with FPOT for a wide range of CH conditions (up to $\rho_{CH} \approx$ 10 g/cm^3). However, *ATOMIC* underestimates the CH opacity by a factor of 2 to 3 for extremely high densities ($\rho_{CH} \geq$ 50 g/cm^3) at which the *ATOMIC* model gives much larger K-edge up-shifting than QMD predictions.

The paper is arranged as follows: The DFT-based QMD method is briefly described in Sec. II, which is followed in Sec. III by a detailed study of K-edge shifting in dense CH plasmas. The established FPOT is compared with the widely used AOT and *ATOMIC* in Sec. III.C, including the total Rosseland mean opacity and the grouped opacity tables. Our conclusions are presented in Sec. IV.

II. THE AB INITIO METHOD FOR X-RAY ABSORPTION IN HED SYSTEMS

Our all-electron QMD calculations were performed with the Vienna *ab initio* simulation package (VASP)[33–35] with electrons treated quantum-mechanically by a plane-wave finite-temperature DFT description. In contrast to most QMD calculations that employ frozen-core pseudopotentials for warm dense CH,[36–40] we represent the electron–ion interaction by the Coulombic potential, $-Z/r$ with $Z = 1$ or $Z = 6$, respectively, for hydrogen and carbon ions. The electron exchange correlation is given by the Perdew–Burke–Ernzerhof (PBE) functional[41] in the generalized-gradient approximation. Under the Born–Oppenheimer approximation, the self-consistent electron density is first determined for a randomly chosen ion configuration by solving the Kohn–Sham DFT equation.[42] Next, the classical ions are moved by the combined electronic and ionic forces, using Newton's equation. This molecular dynamics procedure is repeated for thousands of time steps from which both static and optical properties can be directly evaluated. Finally, the electrons and ions are in thermodynamic equilibrium with equal temperatures ($T_e = T_i$).

Since the pure Coulomb potential describes the electron–ion interactions, we must take high-energy (large-momentum) plane waves in order to sample the tightly bound 1*s*-core electron of carbon. Therefore, we first test the energy cutoff (*ENMAX*) for the plane-wave expansion in solving the Kohn–Sham equation. Figure 1 presents the convergence results for CH at a density of $\rho = 4.0$ g/cm^3 with a temperature of $T = 125{,}000$ K, in which the (a) pressure and (b) internal energy are plotted as a function of the maximum *ENMAX*. In these Γ-point calculations, we have also examined the supercell size effect by varying the number of atoms from $N = 8$ to $N = 54$. Figure 1 indicates that converged static properties of the system can be obtained for *ENMAX* ≥ 40 keV and $N \geq 16$ for which the variation of P and E is within ~1%. This larger energy cutoff is required to accurately sample the deeply bound 1*s* orbital. We used

the energy cutoff of $ENMAX \geq 40$ keV and the number of atoms $N \geq 16$ to calculate all of the all-electron QMD calculations presented in this paper.

After we ran the calculations for thousands of QMD steps, we obtained a sufficient trajectory of ionic configurations. We then chose five to ten uncorrelated snapshots from these ionic configurations to calculate the x-ray absorption spectra of dense CH by computing the velocity dipole matrix elements D_{mn} using the DFT wave functions from VASP. The quantity D_{mn} then determines the frequency-dependent Onsager coefficients via the Kubo–Greenwood formula as[43]

$$L_{ij}(\omega) = \frac{2\pi(-e)^{4-i-j}}{3Vm_e^2\omega}\sum_{mn}F_{mn}|D_{mn}|^2 \times\left(\frac{E_m+E_n}{2}-H\right)^{i+j-2}\delta(E_m-E_n-\mathrm{h}\omega), \quad (1)$$

where $V = 1/\rho$ is the atomic specific volume, E_m (E_n) is the energy of the m-th (n-th) state, and H is the enthalpy (per atom) of the system. The quantity F_{mn} is the difference between the Fermi–Dirac distributions for states m and n at temperature T. To obtain the frequency-dependent absorption coefficient $\alpha_K(\omega)$, we need the electric conductivity and the index of refraction of the system. From the real part of the electric conductivity, $\sigma_1(\omega) = L_{11}(\omega)$ the imaginary part of the electric conductivity can be evaluated from the principal value integral:

$$\sigma_2(\omega) = -\frac{2}{\pi}P\left(\int\frac{\omega\sigma_1(\omega')}{\omega'^2-\omega^2}\mathrm{d}\omega'\right). \quad (2)$$

The dielectric function $e(\omega) = e_1(\omega) + ie_2(\omega)$ can then be calculated by

$$e_1(\omega) = 1 - \frac{4\pi}{\omega}\sigma_2(\omega), \qquad e_2(\omega) = \frac{4\pi}{\omega}\sigma_1(\omega). \tag{3}$$

Using the dielectric function, we obtain the real part of the refraction index:

$$n(\omega) = \sqrt{\frac{|e(\omega)| + e_1(\omega)}{2}}. \tag{4}$$

Finally, the mass-absorption coefficient (α_m) is equal to the absorption coefficient (α_K) divided by the mass density,[44] i.e.,

$$\alpha_m(\omega) = \frac{\alpha_K(\omega)}{\rho} = \frac{4\pi\bar{\sigma}_1(\omega)}{c \times \bar{n}(\omega)} \times \frac{1}{\rho}, \tag{5}$$

with the speed of light c. The "bar" over σ_1 and n stands for averaging over a sample of uncorrelated snapshots. Such ab initio calculations of optical properties[45,46] have been used to build a first-principles opacity table (FPOT) of deuterium for ICF applications.[47] Since the QMD calculations are limited to certain maximum photon energy (due to the number of bands used), we extrapolate the monotonically decreasing high-energy tail of the electrical conductivity

to higher energies, by using a Drude-type fitting formula with an additional ω^3 term described in Ref. [47].

To test the sensitivity of the mass-absorption coefficient to the number of atoms and the *k*-point sampling, we performed a series of tests for dense polystyrene at a density of ρ = 4.0 g/cm^3 and a temperature of T = 125,000 K, which are shown in Fig. 2 for the absorption coefficient as a function of photon energy $h\nu$. For the N = 16 and Γ-point calculations [Fig. 2(a)], we varied the energy cutoff (*ENMAX*) from 20 keV to 60 keV, demonstrating that the overall difference is negligible between *ENMAX* = 40 keV and *ENMAX* = 60 keV, while the *ENMAX* = 20 keV calculation gives a slight energy shift near the K edge of carbon $h\nu \approx 280$ eV. Therefore, setting *ENMAX* ≥ 40 keV should guarantee convergent results. Finally, we plot the *k*-point convergence results in Fig. 2(b) along with a variation in N from N = 16 to N = 32. Compared to the Γ-point-only calculation, a 2 × 2 × 2 Monkhorst–Pack grid gave much smoother results, especially above the carbon K edge. Moreover, the N = 16 calculation (dashed red line) is almost identical to the N = 32 case (solid green line) shown in Fig. 2(b). Therefore, all of our results are from convergent QMD calculations, using *ENMAX* ≥ 40 keV, N ≥ 16, and *k*-point grid of 2 × 2 × 2.

Under the multigroup diffusion approximation, the Rosseland mean opacity K_R is often used for the radiation transport in hydrodynamics simulations. In general, the grouped Rosseland mean opacity is calculated by

$$K_{\mathrm{R}}\left(\omega_1{:}\omega_2\right)=\frac{\displaystyle\int_{\omega_2}^{\omega_1} n\left(\omega\right)^2\frac{\partial B\left(\omega,T\right)}{\partial T}\mathrm{d}\omega}{\displaystyle\int_{\omega_2}^{\omega_1} n\left(\omega\right)^2\frac{1}{\alpha_m\left(\omega\right)}\frac{\partial B\left(\omega,T\right)}{\partial T}\mathrm{d}\omega} \tag{6}$$

for a group of photon energies between $\hbar\omega_1$ and $\hbar\omega_2$. The Planck function,

$$B\left(\omega,T\right)=\frac{\mathrm{h}\omega^3}{4\pi^3c^2}\times\frac{1}{e^{\mathrm{h}\omega/k_BT}-1},$$

depends on the emitting photon energy and the material temperature. We obtain the total/gray Rosseland mean opacity for $\omega_1 = 0$ and $\omega_2 = \infty$.

III. RESULTS AND DISCUSSION

A. Shifting of Carbon K Edge in Highly Compressed Polystyrene

This subsection presents our *ab initio* results for x-ray absorption spectra of CH compressed to densities from $\rho = 4$ g/cm^3 up to $\rho = 100$ g/cm^3. We will focus on understanding the shift of the carbon K edge in highly compressed polystyrene. For the case shown by Figs. 1 and 2, polystyrene was compressed to $\rho = 4$ g/cm^3 with a temperature of $T = 125{,}000$ K. According to Eq. (5), the x-ray absorption coefficient depends on the real parts of the electrical conductivity $\sigma_1(\omega)$ and the refractive index $n(\omega)$. Figure 3 shows the variation of these two quantities with respect to the electromagnetic wave frequency (photon energy). For CH at this condition, the plasma frequency ω_p is so high that the energy associated with plasma oscillation is $\hbar\omega_p \approx 35$ eV. We see from Fig. 3 that the refractive index has a minimum at $\omega = \omega_p$ (strong absorption); $n(\omega)$

increases dramatically for $\omega = \omega_p$ and approaches $n(\omega) = 1$ for $\omega ? \omega_p$, as expected. The electrical conductivity has a relatively small variation at low frequencies, dropping exponentially for $\omega > \omega_p$ until the 1*s*-core electrons become accessible for conduction. The sharp jump of $\sigma_1(\omega)$ at $h\nu = E_K \approx 272$ eV by an order of magnitude indicates the carbon 1*s*-core electrons are involved in conduction (absorption). For $h\nu > E_K$ the electrical conductivity exhibits a monotonic decrease as does the absorption coefficient. The calculated carbon K edge of $E_K \approx 272.3$ eV is about $\Delta E \approx 11.7$ eV smaller than the experimental value in ambient CH. This is a well-known problem in DFT for the PBE exchange-correlation functional, which somewhat underestimates the band gap in general. We have scanned the PBE-DFT calculations from a low CH density of $\rho = 0.1$ g/cm^3 (approaching isolated-atom limit) to $\rho = 1.0$ g/cm^3 and $\rho = 10$ g/cm^3. When the resulting K-edges are compared with experimental K-edge measurements for isolated carbon atom and solid CH, the observed deficit of $\Delta E \approx 11.7$ eV is not significantly changed. Thus, we have added this energy deficit for the K-edges calculated from our PBE calculations (discussed below). We have found that the more accurate hydrid Heyd–Scuseria–Ernzhof (HSE) exchange-correlation functional[48] can provide a much better band gap (ΔE reducing to ~2 eV) but is computationally more time consuming than PBE. In addition, the GW calculations in the "quasi-particle" picture by correcting the self-energy should give more accurate energy levels than the PBE-DFT calculations presented here. However, for our bare Coulomb potentials used here these GW calculations are found to be extremely expensive and memory-demanding, if not impossible, due to the very high cut-off energy (ENCUT > 40-keV) required. Even for the very large computational resources currently available to us (maximum memory of 512 GB per node), we could not obtain reliable GW results at this time.

In Fig. 4, we examine the x-ray absorption spectra of CH compressed to a higher density of $\rho = 10$ g/cm^3 at three temperatures: $T = 31{,}250$ K, 125,000 K, and 500,000 K. Figure 4 indicates that the peak absorption moves to a slightly higher frequency as ω_p shifts up because of the increasing electron density in comparison with the case of $\rho = 4$ g/cm^3 (Fig. 2). For the three temperatures, Fig. 4 shows that the carbon K edge shifts down as the temperature increases from $T = 31{,}250$ K to $T = 500{,}000$ K; the K edge also becomes less steep at higher temperatures (see the inset of Fig. 4). To understand these temperature-induced features of the carbon K edge, we plotted the density of states (DOS's) as a function of energy in Fig. 5 for the three corresponding cases. For the lowest temperature of $T = 31{,}250$ K, the narrow peak at $E \approx -220$ eV is the 1*s*-core electron energy band of carbon ions for 10×-compressed CH. Compared with the 1*s*-core electron binding energy (–282 eV) of an isolated carbon atom, the observed up-shift of core electron energy is caused both by the screening of ionized free electrons to the C^{6+} core and by the microfield influences from surrounding ions. Since we always set the continuum level at $E_C = 0$ in these calculations, the energy up-shifting of 1*s*-core electrons corresponds exactly of the traditional view of "continuum lowering" (or "ionization potential depression"). Namely, the energy gap between the 1*s*-core energy level and the continuum is decreased. At such relatively low temperatures ($T =$ 31,250 K and $T = 125{,}000$ K), the Fermi surface is located at around $E_F \approx 50$ eV (marked by vertical lines in Fig. 5), which means the energy bands below E_F are fully occupied. Therefore, the 1*s*-core electrons can only make a transition to the unoccupied bands above E_F. This determines the K-edge location at $E_K = E_F - E_{1s}$, which accounts exactly for the K edge seen in Fig. 4 (blue and green curves). Because the temperature is well below the Fermi temperature $\left(T < E_F/k\right)$, the Fermi distribution has a sharp cutoff around $E \sim E_F$ so that the lower the temperature, the sharper

the K edge (illustrated by the inset in Fig. 4). When the temperature increases to T = 500,000 K, Fig. 4 shows that the K edge shifts down by ~30 eV (solid red line) with respect to the low-T cases. This is caused by the downshift of the Fermi surface because of thermal excitation of electrons to high-energy bands, as indicated by the dashed red lines in Fig. 5. The 1s band is also significantly broadened as T increases, in which the Fermi-smearing is used to determine the partial occupancies on each orbital. For a fixed density, the K-edge shifting of tens of eV can be used as a measure of material temperature (see the inset in Fig. 4).

Next, we examine the x-ray absorption spectra at even higher densities. The results are plotted in Fig. 6 for CH densities of 10 g/cm^3, 25 g/cm^3, 50 g/cm^3, and 100 g/cm^3 at the same temperature of T = 125,000 K. The black arrow in each panel of Fig. 6 marks the location of the carbon K edge for each situation. One sees that the K edge continuously up-shifts as the density increases, while the contrast of the K edge is gradually reduced. To understand why the K edge shifts in the way shown in Fig. 6, we plot the DOS as a function of band energy in Fig. 7 for the corresponding cases with the vertical dashed line indicating the location of the Fermi surface. Figure 7 shows that (1) the 1s band of the carbon ion moves up and broadens in response to increasing ρ; and (2) the Fermi surface continuously elevates with increasing density (leading to the reduction of absorption caused by Pauli blocking, discussed in the next section). As a consequence, the K edge is again determined by $E_K = E_F + E_C - E_{1s}$ (note that we set the "continuum" at $E_C = 0$). The reduced K-edge contrast can be attributed to the density-induced broadening seen in Fig. 7. For example, the width of the 1s band varies from $\Delta E_{1s} \approx 38$ eV to $\Delta E_{1s} \approx 64$ eV, respectively, for density increasing from $\rho = 25$ g/cm^3 to $\rho = 100$ g/cm^3.

B. The Single-Mixture-In-A-Box (*SMIAB*) Model

Figure 8 plots the carbon K-edge locations from our QMD calculations as a function of the CH density for the same temperature of T = 125,000 K. Our QMD results are represented by the blue diamonds, in which an error bar of $\Delta E \sim 11.7$ eV is assigned to account for the gap inaccuracy of the PBE exchange-correlation functional (discussed above). To test if the traditional density-dependent continuum-lowering models can explain these observations, we compare our QMD results with the different predictions of the carbon K edge in Fig. 8. Four IPD models, including Ecker–Kröll,[8] Stewart–Pyatt,[7] modified ion sphere,[9] and Crowley[11] are used to calculate the carbon K edges with the corresponding mass densities obtained for different ion charge states Z = 1 to 5 by the Fermi–Dirac average-atom model. These IPD models, except the Crowley, did not include the Pauli blocking (degeneracy) effect. We also compare with the *ATOMIC* model.[49–52] *ATOMIC* accounts for IPD by an occupation probability formalism through use of explicitly computed plasma microfields[10] that gradually destroy atomic bound states through field ionization as the density increases. *ATOMIC* also includes an explicit factor that accounts for the rising of the Fermi surface (also known as Pauli blocking[53]) that in this case, causes the carbon K edge to increase. These model predictions are represented by the dashed colored lines with open symbols in Fig. 8. Once again, the K edge for an ion charge state is calculated in these models by $E_K = E_C - E_{1s}$ (isolated), where E_C is the model-predicted IPD and E_{1s} (isolated) is the 1s-electron ionization potential of isolated carbon ion at a charge state of Z. As can be seen from Fig. 8, the first three models predict the K-edge downshifting as ρ_{CH} (Z) increasing, while the Crowley model, taking the electron degeneracy into account, gives a slight up-shift of the K edge, but only for the case of Z = 5. Dramatically different from all four model predictions, our QMD results (blue diamonds) show significant up-shifts for $\rho_{CH} \geq 25$ g/cm^3.

Note that our QMD calculations do not assume what ionization level is reached for each density studied. The *ATOMIC* model also predicts the K-edge up-shifting (caused by the Pauli blocking term discussed earlier) but by a greater amount than the QMD results. For example, at ρ_{CH} = 100 g/cm^3 and T = 125,000 K the carbon K edge from our *ab initio* calculation gives E_K = 422.9 eV (QMD), in contrast to model predictions of E_K = 235.9 eV (Stewart–Pyatt), 76.4 eV (Ecker–Kröll), 136.1 eV (modified ion sphere), 226.6 eV (Crowley), and 613.5 eV (*ATOMIC*), respectively.

To fully understand the physics behind the K-edge up-shifting resulting from our *ab initio* calculations, we have developed a "*single-mixture-in-a-box*" (*SMIAB*) model for strongly coupled fully degenerate plasmas. The *SMIAB* model consists of three components: (1) the continuum-lowering effect on the 1*s*-electron binding energy E_{1s} of targeted carbon ions; (2) the average degree of ionization Z of the mixture determined by an average-atom model;[54] and (3) the rise of the electronic Fermi surface because of compression, which can be calculated by $E_F = \mathrm{h}^2/2m\left(3\pi^2 \times Z \times \rho_{CH}/A_{CH}\right)^{2/3}$ in the case concerned, where $\hbar = h/2\pi$ is the reduced Planck constant, $A_{CH} = \left(A_C + A_H\right)/2$ is the averaged atomic weight of the single mixture (the "basic unit" of polystyrene), and ρ_{CH} is the mass density. To determine the 1*s*-electron binding energy E_{1s} of the carbon ion in a dense polystyrene (ρ_{CH}), we placed the single mixture (one carbon atom and one hydrogen atom) inside a cubic box having a volume of $V = L^3 = A_{CH}/\rho_{CH}$. Using periodic boundary conditions, this simple *SMIAB* picture mimics the microscopic environment of each individual carbon atom experienced in such dense plasmas. We

then calculated the band energy of E_{1s} by self-consistently solving the following Kohn–Sham equation for all N_b electronic orbitals (in atomic units):

$$\left\{-\frac{1}{2}\nabla^2 + V_N(r) + V_H[\rho_e](r) + V_{xc}[\rho_e](r)\right\}\psi_i(r) = E_i\psi_i(r), \tag{7}$$

where V_N represents the electron interactions with both carbon and hydrogen nuclei and the electron density and the Hartree term are defined as

$$\rho_e(r) = \sum_{i=1}^{N_b}|\psi_i(r)|^2; \quad V_H[\rho_e](r) = \int \frac{\rho_e(r')}{|r-r'|}dr'. \tag{8}$$

Since the exchange-correlation term V_{xc} and the Hartree term depend on the electron density $\rho_e(r)$, which is again a function of $\psi_i(r)$, the above Kohn–Sham equation can be solved self-consistently. The PBE exchange-correlation functional is also adopted in the above E_{1s} calculations.

To determine the average ionization Z, we employed the Fermi–Dirac average-atom model with local-density approximation for the exchange-correlation functional. We have applied the equal-pressure mixing rule[55] to gauge the ionization degree from each individual species. For example, for the chosen temperature of T = 125,000 K and a CH density ρ_{CH}, we vary the densities of pure carbon (ρ_C) and pure hydrogen (ρ_H) in the average-atom model to satisfy the following two conditions simultaneously: (1) the equal-pressure condition, e.g., P_C =

P_H; and (2) the additive-volume condition, i.e., $\rho_{CH} = A_{CH}/\left(A_H/\rho_H + A_C/\rho_C\right)$. With these matching conditions, the average-atom model gives the ionization degree (Z_C and Z_H) for each species. Therefore, the average ionization of equimolar CH can be expressed as $Z = \left(Z_C + Z_H\right)/2$. The resulting Z is then used to calculate the elevated Fermi surface. Finally, the K-edge locations are computed for each CH density by $E_K = E_F + E_C – E_{1s} + \Delta E$ (note the continuum is also set to $E_C = 0$). As an example, the *SMIAB* results are listed in Table I for CH at different densities but having the same temperature (T = 125,000 K), which is also plotted in Fig. 8 by the blue solid line. As with the QMD results, we added ΔE = 11.7 eV to the *SMIAB*-predicted carbon K edge, accounting for the inaccuracy of the PBE functional for energy-gap calculations.

From Fig. 8 one can see that this simple *SMIAB* model does a much better job than all other continuum-lowering models at explaining the QMD results (within an error of ±15 eV), indicating that the *SMIAB* with periodic boundary conditions can predict the continuum lowering of atomic ions affected by surrounding ions/electrons in a dense material. Moreover, the rising of the Fermi surface, estimated from the average-atom model, reproduces well the essence of electron degeneracy in such systems while the existing models failed to predict the K-edge locations in such strongly coupled and fully degenerate dense materials. A similar model[56] (*SMIAB*) also explains the K-edge shifting in extremely dense pure carbon plasmas. We anticipate that the simple *SMIAB* model will find important applications in studying HED properties of extremely dense materials. For example, one can use this simple model to infer density of higly compressed materials from experimental K-edge measurements. It is noted that the traditional continuum lowering models, including Ecker–Kröll, Stewart–Pyatt, and modified

ion sphere, did not include the Pauli blocking (degeneracy) effect; Adding the Pauli blocking effect from our average-atom model to these continuum-lowering models still results in different K-edge locations from our QMD calculations and *SMIAB* model predictions.

C. Opacity Comparisons Between QMD and Other Models

For ICF and HED applications, we have extended our QMD calculations of opacity to cover a wide range of CH in the warm-dense-matter regime. Specifically, we have scanned the CH density from $\rho_{CH} = 0.1$ g/cm^3 to $\rho_{CH} = 100$ g/cm^3 with the temperature range of $T = 2000$ to 1,000,000 K. To make a global opacity table, we first compare the QMD-calculated opacity with model predictions. Two opacity models are compared here: (1) the AOT[31] and (2) the *ATOMIC* model,[32] which contains improvements to the free–free opacity contribution compared to earlier work.[49] *ATOMIC* is designed to produce opacities over very large ranges of temperatures and densities and are most commonly used for astrophysical modeling at low and moderate densities as well as in radiation–hydrodynamics codes for simulations of ICF and HED experiments. Still, it is of interest to explore how these *ATOMIC* opacities compare at the high (compressed) densities studied here.

ATOMIC is a multipurpose opacity and kinetics code,[50] which has been recently used to generate new Los Alamos OPLIB tables for hydrogen through zinc[49] that employs atomic data from the Los Alamos suite of atomic physics codes[51] and an equation of state (known as ChemEOS) based on a chemical picture.[52] Recently, improvements to the free–free component of the opacity in *ATOMIC* have been implemented[32] based on enforcement of the conductivity sum rule,[57] which resulted in excellent agreement between *ATOMIC* calculations, DFT–

molecular dynamics (MD) simulations,[47] and pseudo-atom potential calculations[58] for the opacity of deuterium. For the CH opacity studied here, a multi-element procedure[59] was used within *ATOMIC* that iterates to ensure a self-consistent free-electron density for a specified temperature and mass density of the constituent elements.

We first compare the QMD results (red lines) with the *ATOMIC* predictions (green dashed lines) in Figs. 9 and 10 for CH densities varying from ρ_{CH} = 4 g/cm^3 to ρ_{CH} = 100 g/cm^3 at T = 125,000 K, in which the absorption coefficient α_K is plotted as a function of x-ray photon energy $h\nu$. At relatively low densities (ρ_{CH} = 4 g/cm^3 and ρ_{CH} = 10 g/cm^3), Figure 9 shows that the improved *ATOMIC* model agrees overall with QMD in the entire photon energy range. Some detailed differences near the K edge are noticed; for example, the *ATOMIC* model shows the existence of the 1s → 2p peak (before K edge) while QMD gives smooth K edges without distinct bound–bound transition peaks. We argue that the density effect, represented *naturally* in the *ab initio* QMD calculations, has made the 2p states of carbon emerge into the continuum. Again, the observed K-edge energy difficit (ΔE) in QMD is caused by the use of PBE exchange-correlation functional (discussed above). When the CH density is further increased to ρ_{CH} = 50 g/cm^3 [Fig. 10(a)] and ρ_{CH} = 100 g/cm^3 [Fig. 10(b)], the carbon K-edge shifts are significantly different between QMD and *ATOMIC* predictions. For example, Fig. 10(a) indicates that for ρ_{CH} = 50 g/cm^3, the QMD-predicted carbon K edge is located at E_K = 349.8 eV, while, in contrast, the *ATOMIC* model gives E_K = 510.8 eV. The difference in the carbon K-edge shift between QMD and *ATOMIC* is further increased for the highest density (ρ_{CH} = 100 g/cm^3). As previously discussed, the *ATOMIC* model includes the competing effects of IPD (from an occupation probability consideration[49]) that lower the K edge, and the Fermi

surface rising[50] that increases the K edge. Both of these effects are density dependent, and it is not yet clear which effect is responsible for the difference found with the QMD results.

Next, we compare the total/gray Rosseland mean opacity K_R of CH in Figs. 11 and 12, calculated by Eq. (6) for different CH densities. In these figures, the total Rosseland mean opacity is plotted as a function of CH temperature. Figures 11(a) and 11(b) show the cases for ρ_{CH} = 0.5 g/cm^3 and ρ_{CH} = 4.0 g/cm^3, respectively. Besides the QMD and *ATOMIC* results, we have also added the AOT predictions. Historically, the AOT model had been used to simulate ICF and HED experiments.[60–63] The data in AOT table were limited to certain temperatures for dense materials, below which the cold opacity was usually "patched in" to enable radiation hydro simulations. Figure 11(a) indicates that for relatively low CH density (ρ_{CH} = 0.5 g/cm^3), all three (QMD, *ATOMIC*, and AOT) predictions agree with each other as the temperature increases; for $T <$ 10 eV, the cold-opacity patched AOT underestimates K_R by more than an order of magnitude in comparison with QMD and *ATOMIC*. The latter two results are almost identical to each other for a temperature as low as ~5.39 eV although a factor of ~2 difference is observed at T . 2.69 eV. For low temperatures and moderate densities, convergence of the *ChemEOS* model is often more difficult to obtain. Also, the role of negative-ion formation and its effect both on the EOS and opacity require further scrutiny. At ρ_{CH} = 4.0 g/cm^3, Fig. 11(b) shows a similar situation: the improved *ATOMIC* model gives overall good agreement with QMD predictions, although some differences are seen for T = 40 to 100 eV.

For higher densities of ρ_{CH} = 10 g/cm^3 and ρ_{CH} = 50 g/cm^3, Fig. 12 shows a trend similar to that in Fig. 11. Namely, the cold-opacity patched to AOT generally underestimates the Rosseland opacity of warm dense CH by a factor of ~10 at low temperatures. The improved

ATOMIC model gives a good account of the enhanced opacity in QMD calculations for $\rho_{CH} \leq$ 10 g/cm^3. Again, some differences between QMD and *ATOMIC* are still seen for the relatively high-T regime ($T \sim$ 40 to 100 eV). This may be attributed to the detailed differences near the carbon K edge (see Figs. 9 and 10) since the Rosseland mean opacity weighs more around $h\nu \approx 4$ kT [i.e., the peak of $\partial B(\omega,T)/\partial T$]. Consequently, Fig. 12(b) further shows a larger K_R difference between QMD and *ATOMIC* for the higher CH density of ρ_{CH} = 50 g/cm^3. This is consistent with the K-edge shifting difference seen in Fig. 10(a). Again, the K_R difference is within a factor of ~2, between QMD and *ATOMIC*, but overall higher than the cold-opacity patched to AOT.

Finally, we compare the grouped Rosseland mean opacities between QMD and AOT in Figs. 13 and 14, for CH densities of ρ_{CH} = 4 g/cm^3 and ρ_{CH} = 50 g/cm^3, respectively. As we discussed above, AOT has been extensively used for radiation–hydrodynamics simulations of ICF/HED experiments. Forty-eight photon-energy groups are normally used for CH simulations. Therefore, we compare our QMD results with AOT in these figures with the same 48 energy groups. In Fig. 13, the four panels display the grouped Rosseland mean opacities as a function of photon energy in each group for temperatures varying from (a) T = 62,500 K to (d) T = 1,000,000 K. One sees from Fig. 13 that for $T <$ 500,000 K, the first and second energy groups ($h\nu \leq$ 100 eV) are largely different between QMD and AOT; the opacities for high-energy groups above the carbon K edge are almost identical between the two models, although some small differences are seen near the K-edge groups. For a higher density of ρ_{CH} = 50 g/cm^3, Fig. 14 shows significant differences between QMD and AOT: (1) the QMD opacities of low-energy groups below K edge ($h\nu \leq$ 285 eV) are 10× higher than the cold-opacity patched to

AOT; and (2) the K-edge shifting predicted by QMD is totally absent in AOT. As the temperature increases, our QMD results indicate that the carbon K edge gradually becomes less pronounced and eventually disappears at T = 1,000,000 K in such a dense polystyrene, shown by Fig. 14(d). This is expected since the 1*s*-core electrons become free (ionized) as T and ρ increase. On the contrary, the AOT model persistently gives the sharp and unshifted K edge of carbon. We expect that these differences will affect radiation transport of low-energy ($h\nu \leq$ 400 eV) photons in ICF/HED simulations.

IV. CONCLUSION

We have used the DFT-based QMD method to perform *ab initio* studies on the x-ray absorption properties of highly compressed CH. These first-principles QMD studies are made possible by using the all-electron pure Coulombic potentials, which are in contrast to most frozen-core pseudopotential DFT calculations. We found that as CH is compressed to larger and larger densities, the carbon K-edge is up-shifted significantly, which was missing in traditional IPD models. The *ATOMIC* model, which includes IPD effects and the rising of the Fermi surface, also predicts the K-edge up-shifting, but to a larger degree than the QMD calculations. In addition, we have developed a physics-based *SMIAB* model to understand the observed carbon K-edge shifting from our QMD calculations. The simple *SMIAB* picture reveals that for strongly coupled and fully degenerate dense CH, the carbon K edge is essentially determined by both the lowering of the ionization potential of carbon ion and the rising of the electronic Fermi surface resulting from the compression in dense CH. *SMIAB* gives good agreement with the *ab initio* results from detailed and large-scale QMD calculations. Such a simple *SMIAB* model might

provide guidance for inferring density/temperature conditions from K-edge–shifting-measurements in extremely dense materials.

These *ab initio* calculations have been expanded to a wide range of CH densities and temperatures. The resulting FPOT was compared with two extensively used opacity models (AOT and *ATOMIC*). We found that the cold-opacity–patched AOT generally underestimated the CH opacity by an order of magnitude for warm, dense polystyrene while the improved *ATOMIC* model gave a good account for the enhanced opacity seen in QMD for relatively dense CH ($\rho_{CH} \leq 10$ g/cm^3) in the low-temperature regime ($T < 20$ eV). As the CH density further increases to $\rho_{CH} \geq 50$ g/cm^3, however, the *ATOMIC* model gives a factor of ~2 lower opacity when compared to our QMD results because of an overestimate of the shift of the K edge in *ATOMIC*. Finally, the comparisons between our QMD results with the extensively used AOT clearly indicate that the Rosseland mean opacities in low-photon energy groups (below K edge) can differ by a factor of ~10. We anticipate that these detailed differences will affect the radiation transport of soft x-ray photons in simulations of ICF and HED experiments. We hope such detailed studies will facilitate experimental measurements, in particular, of the observable K-edge shifting in extremely dense materials.

Note Added: After our manuscript was submitted, an interesting research paper [64] on K_α , K_β, and K-edge shifts of Fe in dense Be plasmas was published, in which the DFT-based model (MUZE: similar to our SMIAB discussed here) properly explained the observed line/edge shifting in experiments.

Acknowledgment

This material is based upon work supported by the Department of Energy National Nuclear Security Administration under Award Number DE-NA0001944, the University of Rochester, and the New York State Energy Research and Development Authority. The support of DOE does not constitute an endorsement by DOE of the views expressed in this article. This work was also supported by Scientific Campaign 10 at the Los Alamos National Laboratory, operated by Los Alamos National Security, LLC for the National Nuclear Security Administration of the U.S. Department of Energy under Contract No.#DE-AC52-06NA25396.

This report was prepared as an account of work sponsored by an agency of the U.S. Government. Neither the U.S. Government nor any agency thereof, nor any of their employees, makes any warranty, express or implied, or assumes any legal liability or responsibility for the accuracy, completeness, or usefulness of any information, apparatus, product, or process disclosed, or represents that its use would not infringe privately owned rights. Reference herein to any specific commercial product, process, or service by trade name, trademark, manufacturer, or otherwise does not necessarily constitute or imply its endorsement, recommendation, or favoring by the U.S. Government or any agency thereof. The views and opinions of authors expressed herein do not necessarily state or reflect those of the U.S. Government or any agency thereof.

References

[1]S. B. Hansen, A. Ya. Faenov, T. A. Pikuz, K. B. Fournier, R. Shepherd, H. Chen, K. Widmann, S. C. Wilks, Y. Ping, H. K. Chung *et al.*, Phys. Rev. E **72**, 035608 (2005).

[2]S. Mazevet and G. Zérah, Phys. Rev. Lett. **101**, 155001 (2008).

[3]V. Recoules, F. Lambert, A. Decoster, B. Canaud, and J. Clérouin, Phys. Rev. Lett. **102**, 075002 (2009).

[4]J. E. Bailey, T. Nagayama, G. P. Loisel, G. A. Rochau, C. Blancard, J. Colgan, Ph. Cosse, G. Faussurier, C. J. Fontes, F. Gilleron *et al.*, Nature **517**, 56 (2015).

[5]F. Dorchies, F. Festa, V. Recoules, O. Peyrusse, A. Benuzzi-Mounaix, E. Brambrink, A. Levy, A. Ravasio, M. Koenig, T. Hall *et al.*, Phys. Rev. B **92**, 085117 (2015).

[6]S. Zhang, S. Zhao, W. N. Kang, P. Zhang, and X.-T. He, Phys. Rev. B **93**, 115114 (2016).

[7]J. C. Stewart and K. D. Pyatt, Jr., Astrophys. J. **144**, 1203 (1966).

[8]G. Ecker and W. Kröll, Phys. Fluids **6**, 62 (1963).

[9]D. Liberman and J. Albritton, J. Quant. Spectrosc. Radiat. Transf. **51**, 197 (1994).

[10]D. G. Hummer and D. Mihalas, Astrophys. J. **331**, 794 (1988).

[11]B. J. B. Crowley, Phys. Rev. A **41**, 2179 (1990).

[12]S. J. Rose, J. Phys. B: At. Mol. Opt. Phys. **25**, 1667 (1992).

[13]W. F. Huebner and W. D. Barfield, *Opacity*, Vol. 402 (Springer, New York, 2014).

[14]C. A. Iglesias and F. J. Rogers, Astrophys. J. **464**, 943 (1996).

[15]S. M. Vinko, O. Ciricosta, B. I. Cho, K. Engelhorn, H. K. Chung, C. R. D. Brown, T. Burian, J. Chalupsky, R. W. Falcone, C. Graves *et al.*, Nature **482**, 59 (2012).

[16]O. Ciricosta, S. M. Vinko, H. K. Chung, B. I. Cho, C. R. D. Brown, T. Burian, J. Chalupský, K. Engelhorn, R. W. Falcone, C. Graves *et al.*, Phys. Rev. Lett. **109**, 065002 (2012).

[17]D. J. Hoarty, P. Allan, S. F. James, C. R. D. Brown, L. M. R. Hobbs, M. P. Hill, J. W. O. Harris, J. Morton, M. G. Brookes, R. Shepherd *et al.*, Phys. Rev. Lett. **110**, 265003 (2013).

[18]L. B. Fletcher, A. L. Kritcher, A. Pak, T. Ma, T. Döppner, C. Fortmann, L. Divol, O. S. Jones, O. L. Landen, H. A. Scott *et al.*, Phys. Rev. Lett. **112**, 145004 (2014).

[19]O. Ciricosta, S. M. Vinko, B. Barbrel, D. S. Rackstraw, T. R. Preston, T. Burian, J. Chalupsky, B. I. Cho, H. K. Chung, G. L. Dakovski *et al.*, Nat. Commun. **7**, 11713 (2016).

[20]S.-K. Son, R. Thiele, Z. Jurek, B. Ziaja, and R. Santra, Phys. Rev. X **4**, 031004 (2014).

[21]B. J. B. Crowley, High Energy Density Phys. **13**, 84 (2014).

[22]S. B. Hansen, J. Colgan, A. Ya. Faenov, J. Abdallah, Jr., S. A. Pikuz Jr., I. Yu. Skobelev, E. Wagenaars, N. Booth, O. Culfa, R. J. Dance *et al.*, Phys. Plasmas **21**, 031213 (2014).

[23]C. A. Iglesias, High Energy Density Phys. **12**, 5 (2014).

[24]V. N. Goncharov, T. C. Sangster, T. R. Boehly, S. X. Hu, I. V. Igumenshchev, F. J. Marshall, R. L. McCrory, D. D. Meyerhofer, P. B. Radha, W. Seka *et al.*, Phys. Rev. Lett. **104**, 165001 (2010).

[25]S. W. Haan, J. D. Lindl, D. A. Callahan, D. S. Clark, J. D. Salmonson, B. A. Hammel, L. J. Atherton, R. C. Cook, M. J. Edwards, S. Glenzer *et al.*, Phys. Plasmas **18**, 051001 (2011).

[26]D. D. Meyerhofer, R. L. McCrory, R. Betti, T. R. Boehly, D. T. Casey, T. J. B. Collins, R. S. Craxton, J. A. Delettrez, D. H. Edgell, R. Epstein *et al.*, Nucl. Fusion **51**, 053010 (2011).

[27]V. N. Goncharov, T. C. Sangster, R. Betti, T. R. Boehly, M. J. Bonino, T. J. B. Collins, R. S. Craxton, J. A. Delettrez, D. H. Edgell, R. Epstein *et al.*, Phys. Plasmas **21**, 056315 (2014).

[28]R. Betti and O. A. Hurricane, Nat. Phys. **12**, 435 (2016).

[29]S. X. Hu, B. Militzer, V. N. Goncharov, and S. Skupsky, Phys. Rev. Lett. **104**, 235003 (2010).

[30]S. X. Hu, B. Militzer, V. N. Goncharov, and S. Skupsky, Phys. Rev. B **84**, 224109 (2011).

[31]W. F. Huebner, A. L. Merts, N. H. Magee, Jr., and M. F. Argo, Los Alamos National Laboratory, Los Alamos, NM, Report LA-6760-M (1977).

[32]N. R. Shaffer, N. G. Ferris, J. Colgan, D. P. Kilcrease, and C. E. Starrett, High Energy Density Phys. **23**, 31 (2017).

[33]G. Kresse and J. Hafner, Phys. Rev. B **47**, 558 (1993).

[34]G. Kresse and J. Hafner, Phys. Rev. B **49**, 14,251 (1994).

[35]G. Kresse and J. Furthmüller, Phys. Rev. B **54**, 11,169 (1996)

[36]S. Hamel, L. X. Benedict, P. M. Celliers, M. A. Barrios, T. R. Boehly, G. W. Collins, T. Döppner, J. H. Eggert, D. R. Farley, D. G. Hicks *et al.*, Phys. Rev. B **86**, 094113 (2012).

[37]S. X. Hu, T. R. Boehly, and L. A. Collins, Phys. Rev. E **89**, 063104 (2014).

[38]S. X. Hu, L. A. Collins, V. N. Goncharov, J. D. Kress, R. L. McCrory, and S. Skupsky, Phys. Rev. E **92**, 043104 (2015).

[39]G. Huser, V. Recoules, N. Ozaki, T. Sano, Y. Sakawa, G. Salin, B. Albertazzi, K. Miyanishi, and R. Kodama, Phys. Rev. E **92**, 063108 (2015).

[40]S. X. Hu, L. A. Collins, V. N. Goncharov, J. D. Kress, R. L. McCrory, and S. Skupsky, Phys. Plasmas **23**, 042704 (2016).

[41] J. P. Perdew, K. Burke, and M. Ernzerhof, Phys. Rev. Lett. **77**, 3865 (1996); *ibid* **78**, 1396(E) (1997);

[42]W. Kohn and L. J. Sham, Phys. Rev. **140**, A1133 (1965).

[43]R. Kubo, J. Phys. Soc. Jpn. **12**, 570 (1957); D. A. Greenwood, Proc. Phys. Soc. Lond. **71**, 585 (1958).

[44]F. Perrot, Laser Part. Beams **14**, 731 (1996).

[45]L. A. Collins, S. R. Bickham, J. D. Kress, S. Mazevet, T. J. Lenosky, N. J. Troullier, and W. Windl, Phys. Rev. B **63**, 184110 (2001).

[46]S. Mazevet, L. A. Collins, N. H. Magee, J. D. Kress, and J. J. Keady, Astron. Astrophys. **405**, L5 (2003).

[47]S. X. Hu, L. A. Collins, V. N. Goncharov, T. R. Boehly, R. Epstein, R. L. McCrory, and S. Skupsky, Phys. Rev. E **90**, 033111 (2014).

[48]J. Heyd, G. E. Scuseria, and M. Ernzerhof, J. Chem. Phys. **118**, 8207 (2003).

[49]J. Colgan, D. P. Kilcrease, N. H. Magee, M. E. Sherrill, Jr. Abdallah, J., P. Hakel, C. J. Fontes, J. A. Guzik, and K. A. Mussack, Astrophys. J. **817**, 116 (2016).

[50] N. H. Magee, J. Abdallah, J. Colgan, P. Hakel, D. P. Kilcrease, S. Mazevet, M. Sherrill, C. J. Fontes, and H. L. Zhang, AIP Conf. Proc. **730**, 168 (2004); P. Hakel, M. E. Sherrill, S. Mazevet, J. Abdallah, J. Colgan, D. P. Kilcrease, N. H. Magee, C. J. Fontes, and H. L. Zhang, J. Quant. Spectrosc. Radiat. Transf. **99**, 265 (2006).

[51]C. J. Fontes, H. L. Zhang, J. Abdallah, Jr., R. E. H. Clark, D. P. Kilcrease, J. Colgan, R. T. Cunningham, P. Hakel, N. H. Magee, and M. E. Sherrill, J. Phys. B: At. Mol. Opt. Phys. **48**, 144014 (2015).

[52]P. Hakel and D. P. Kilcrease, AIP Conf. Proc. **730**, 190 (2004).

[53]A. N. Cox, in *Stars and Stellar Systems*, edited by L. H. Aller and D. B. McLaughlin, Stellar Structure, Vol. VIII, edited by G. P. Kuiper and B. M. Middlehurst (The University of Chicago, Chicago, 1965), p. 212.

[54]F. Lambert, J. Clérouin, J.-F. Danel, L. Kazandjian, and G. Zérah, Phys. Rev. E **77**, 026402 (2008).

[55]F. Lambert, J. Clérouin, and G. Zérah, Phys. Rev. E **73**, 016403 (2006).

[56]S. X. Hu, Phys. Rev. Lett. **119**, 065001 (2017).

[57]W. R. Johnson, C. Guet, and G. F. Bertsch, J. Quant. Spectrosc. Radiat. Transf. **99**, 327 (2006).

[58]C. E. Starrett and D. Saumon, High Energy Density Phys. **10**, 35 (2014).

[59]M. E. Sherrill, R. C. Mancini, J. Bailey, A. Filuk, B. Clark, P. Lake, and J. Abdallah, Jr., Phys. Rev. E **76**, 056401 (2007).

[60]T. J. B. Collins, J. A. Marozas, K. S. Anderson, R. Betti, R. S. Craxton, J. A. Delettrez, V. N. Goncharov, D. R. Harding, F. J. Marshall, R. L. McCrory *et al.*, Phys. Plasmas **19**, 056308 (2012).

[61]S. X. Hu, P. B. Radha, J. A. Marozas, R. Betti, T. J. B. Collins, R. S. Craxton, J. A. Delettrez, D. H. Edgell, R. Epstein, V. N. Goncharov *et al.*, Phys. Plasmas **16**, 112706 (2009).

[62]S. X. Hu, V. N. Goncharov, P. B. Radha, J. A. Marozas, S. Skupsky, T. R. Boehly, T. C. Sangster, D. D. Meyerhofer, and R. L. McCrory, Phys. Plasmas **17**, 102706 (2010).

[63]S. X. Hu, D. T. Michel, D. H. Edgell, D. H. Froula, R. K. Follett, V. N. Goncharov, J. F. Myatt, S. Skupsky, and B. Yaakobi, Phys. Plasmas **20**, 032704 (2013).

[64]S. B. Hansen, E. C. Harding, P. F. Knapp, M. R. Gomez, T. Nagayama, J. E. Bailey, High Energy Density Physics **24**, 39 (2017).

Figure captions

FIG. 1. (Color online) Results of convergence tests for polystyrene (CH) at ρ = 4.0 g/cm^3 and T = 125,000 K: (a) pressure and (b) internal energy as a function of the energy cutoff (*ENMAX*) and the number of atoms (N) in the supercell. The pure Coulombic potentials are used in our *all-electron* quantum-molecular-dynamics (QMD) calculations. The convergence of static properties is generally reached for *ENMAX* ≥ 40 keV and $N \geq 16$.

FIG. 2. (Color online) Convergence testing results of x-ray absorption spectra for CH at ρ = 4.0 g/cm^3 and T = 125,000 K: (a) *ENMAX* varying from 20 keV to 60 keV with 16-atom and Γ-point calculations; (b) changing the number of atoms and k point with *ENMAX* = 40 keV. Convergence of x-ray absorption calculations is generally reached for *ENMAX* ≥ 40 keV and $N \geq 16$.

FIG. 3. (Color online) The electrical conductivity and the refractive index are plotted as functions of the photon energy (frequency) for the case of polystyrene at ρ = 4.0 g/cm^3 and T = 125,000 K.

FIG. 4. (Color online) The x-ray absorption coefficient α_K is plotted as a function of the photon energy (frequency) for CH at a higher density of ρ = 10 g/cm^3 with temperatures varying from T = 31,250 K to T = 500,000 K. The small K-edge movement is seen for the highest temperature case of T = 500,000 K (dashed red line).

FIG. 5. (Color online) The density of state (DOS) is plotted for each corresponding case shown in Fig. 4. The Fermi-energy levels are marked by the vertical lines for each case. The downshift of the Fermi surface at T = 500,000 K explains the K-edge movement seen in Fig. 4 (dashed red line) at this higher temperature.

FIG. 6. (Color online) The x-ray absorption spectra are plotted as a function of the photon energy (frequency) for CH at different densities varying from (a) ρ = 10 g/cm^3 to (d) ρ = 100 g/cm^3 with a fixed temperature of T = 125,000 K. The K-edge up-shifting with CH density increasing is clearly seen.

FIG. 7. (Color online) The DOS for each corresponding case shown in Fig. 6. Again, the vertical dashed line in each panel marks the Fermi surface location for each case.

FIG. 8. (Color online) The QMD-predicted K edges of carbon are plotted as a function of CH density. Predictions from five different continuum-lowering models, including the Stewart–Pyatt,[7] Ecker–Kröll model,[8] the modified ion-sphere model,[9] Crowley,[11] and the newly improved *ATOMIC* code (Los Alamos) using the Hummer–Mihalas continuum-lowering model[10] with the consideration of Pauli blocking, are also drawn in the same figure by dashed

lines with open symbols. The "single-mixture-in-a-box" (*SMIAB*), developed in this work, is indicated by the blue solid line.

FIG. 9. (Color online) Comparisons of the absorption coefficient α_K of polystyrene as a function of photon energy $h\nu$ between our QMD calculations and LANL's newly improved *ATOMIC* model are made for densities of (a) $\rho = 4$ g/cm^3 and (b) $\rho = 10$ g/cm^3, both at $T = 125{,}000$ K.

FIG. 10. (Color online) Similar to Fig. 9 but for CH densities of (a) $\rho = 50$ g/cm^3 and (b) $\rho = 100$ g/cm^3 both at $T = 125{,}000$ K.

FIG. 11. (Color online) Comparisons of Rosseland mean opacity (KR) as a function of CH temperature, among our QMD calculations, the LANL's *ATOMIC* model, and the cold-opacity–patched astrophysics opacity table (AOT), are made for CH densities of (a) $\rho = 0.5$ g/cm^3 and (b) $\rho = 4.0$ g/cm^3.

FIG. 12. (Color online) Similar to Fig. 11 but for CH densities of (a) $\rho = 10$ g/cm^3 and (b) $\rho = 50$ g/ cm^3.

FIG. 13. (Color online) The grouped Rosseland opacities, from both our QMD calculations and AOT, are plotted as a function of x-ray photon energy ($h\nu$) for a fixed CH density of $\rho = 4$ g/cm^3, but at different temperatures of (a) $T = 62{,}500$ K, (b) $T = 125{,}000$ K, (c) $T = 500{,}000$ K, and (d) $T = 1{,}000{,}000$ K.

FIG. 14. (Color online) The grouped Rosseland opacities, from both our QMD calculations and AOT, are plotted as a function of x-ray photon energy ($h\nu$) for a much higher CH density of ρ = 50 g/cm^3 and at different temperatures of (a) T = 125,000 K, (b) T = 250,000 K, (c) T = 500,000 K and (d) T = 1,000,000 K.

Tables

Table I: The predicted carbon K edges (with ΔE = 11.7-eV shift) by the single-mixture-in-a-box (*SMIAB*) model for polystyrene (CH) at different densities with a fixed temperature of T = 125,000 K. Z and E_F are the average charge of CH and the electron Fermi energy, respectively.

Density (g/cm^3)	E_{1s} (eV)	Z	E_F (eV)	$E_{K\ edge}$
1	–268.2	1.20	8.7	288.6
4	–245.5	1.47	24.3	281.5
10	–220.1	1.79	51.0	282.8
25	–179.5	2.12	105.8	297.0
50	–142.2	2.37	179.7	333.6
100	–93.5	2.59	302.7	407.9
150	–58.5	2.69	407.4	477.6

FIG. 1.

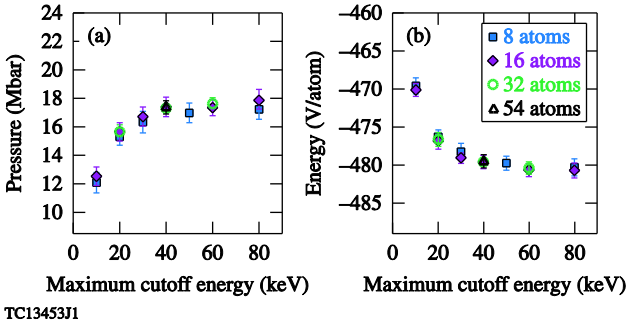
(a)
(b)
Pressure (Mbar)
Energy (V/atom)
Maximum cutoff energy (keV)
Maximum cutoff energy (keV)
8 atoms
16 atoms
32 atoms
54 atoms
TC13453J1

FIG. 2.

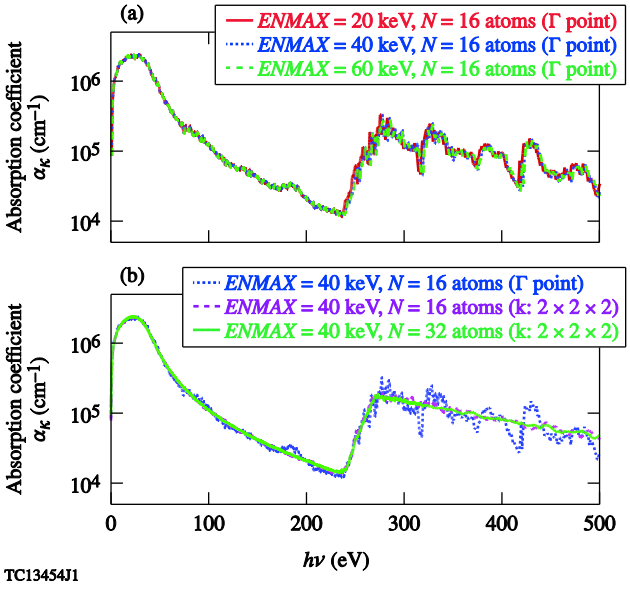
(a)
ENMAX = 20 keV, N = 16 atoms (Γ point)
ENMAX = 40 keV, N = 16 atoms (Γ point)
ENMAX = 60 keV, N = 16 atoms (Γ point)
Absorption coefficient
α_κ (cm^{-1})
10^6
10^5
10^4
(b)
ENMAX = 40 keV, N = 16 atoms (Γ point)
ENMAX = 40 keV, N = 16 atoms (k: 2 × 2 × 2)
ENMAX = 40 keV, N = 32 atoms (k: 2 × 2 × 2)
Absorption coefficient
α_κ (cm^{-1})
10^6
10^5
10^4
0
100
200
300
400
500
$h\nu$ (eV)
TC13454J1

FIG. 3.

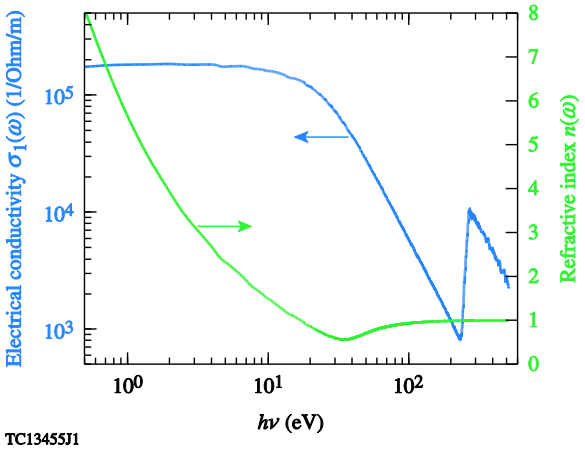
Electrical conductivity $\sigma_1(\omega)$ (1/Ohm/m)
10^5
10^4
10^3
10^0
10^1
10^2
$h\nu$ (eV)
Refractive index $n(\omega)$
8
7
6
5
4
3
2
1
0
TC13455J1

FIG. 4.

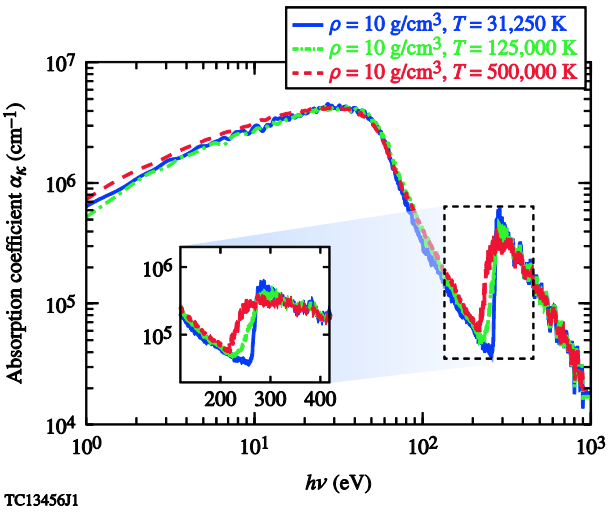
ρ = 10 g/cm3, T = 31,250 K
ρ = 10 g/cm3, T = 125,000 K
ρ = 10 g/cm3, T = 500,000 K
Absorption coefficient ακ (cm−1)
hν (eV)
TC13456J1

FIG. 5.

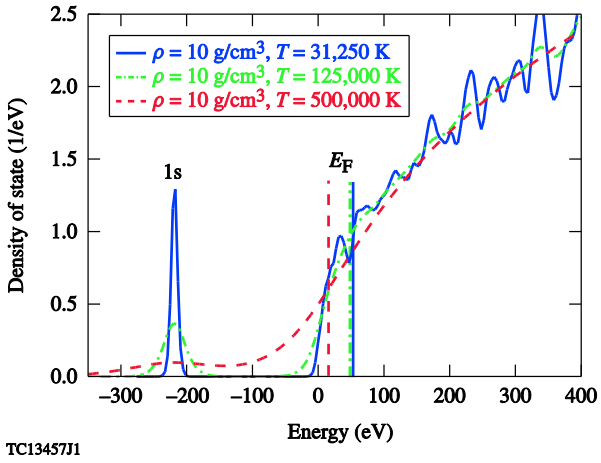
ρ = 10 g/cm3, T = 31,250 K
ρ = 10 g/cm3, T = 125,000 K
ρ = 10 g/cm3, T = 500,000 K
1s
EF
Density of state (1/eV)
Energy (eV)
2.5
2.0
1.5
1.0
0.5
0.0
–300
–200
–100
0
100
200
300
400
TC13457J1

FIG. 6.

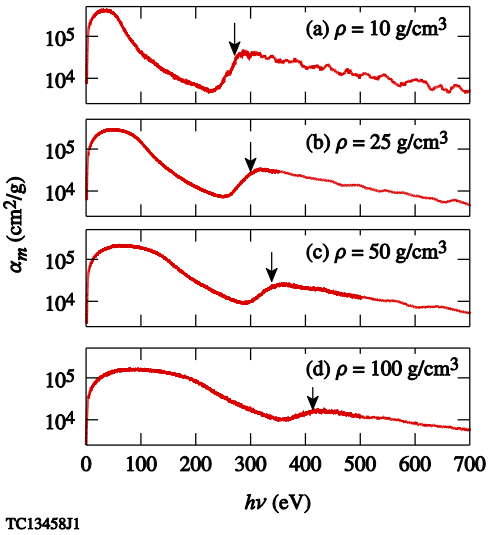
(a) ρ = 10 g/cm3
(b) ρ = 25 g/cm3
(c) ρ = 50 g/cm3
(d) ρ = 100 g/cm3
10^5
10^4
α_m (cm^2/g)
0
100
200
300
400
500
600
700
hν (eV)
TC13458J1

FIG. 7.

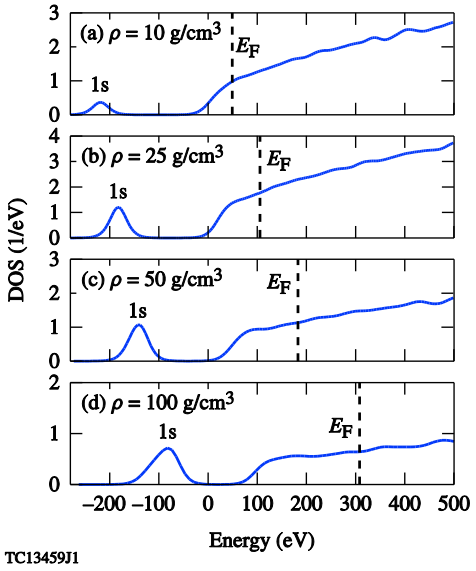
(a) ρ = 10 g/cm3
(b) ρ = 25 g/cm3
(c) ρ = 50 g/cm3
(d) ρ = 100 g/cm3
1s
EF
DOS (1/eV)
Energy (eV)
TC13459J1

FIG. 8.

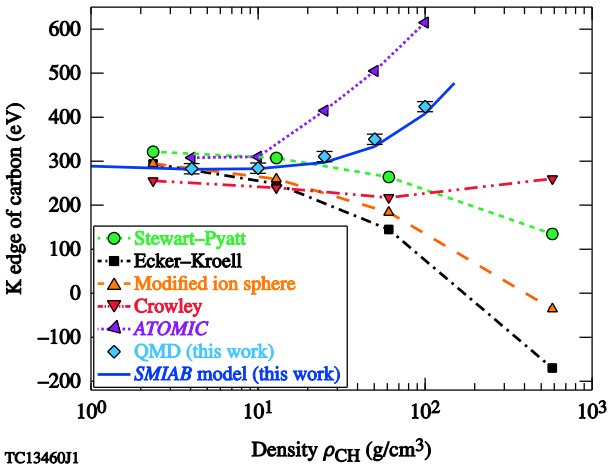
600
500
400
300
200
100
0
–100
–200
K edge of carbon (eV)
Stewart–Pyatt
Ecker–Kroell
Modified ion sphere
Crowley
ATOMIC
QMD (this work)
SMIAB model (this work)
10^0
10^1
10^2
10^3
Density ρCH (g/cm3)
TC13460J1

FIG. 9.

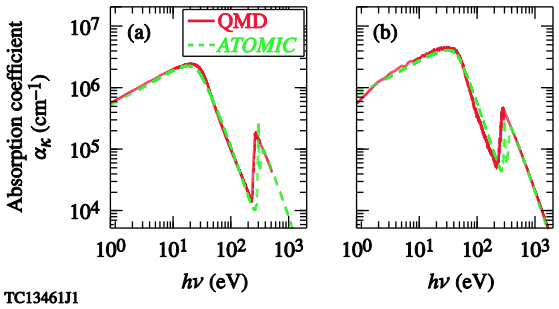
Absorption coefficient
α_K (cm^{-1})
10^7
10^6
10^5
10^4
(a)
QMD
ATOMIC
10^0
10^1
10^2
10^3
$h\nu$ (eV)
(b)
10^0
10^1
10^2
10^3
$h\nu$ (eV)
TC13461J1

FIG. 10.

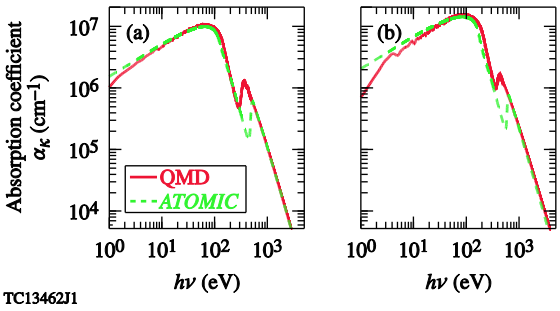
Absorption coefficient
α_κ (cm^{-1})
10^7
10^6
10^5
10^4
(a)
QMD
ATOMIC
10^0 10^1 10^2 10^3
$h\nu$ (eV)
(b)
10^0 10^1 10^2 10^3
$h\nu$ (eV)
TC13462J1

FIG. 11.

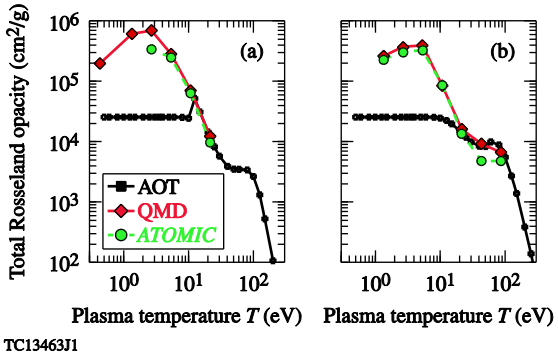
Total Rosseland opacity (cm²/g)
10⁶
10⁵
10⁴
10³
10²
(a)
(b)
AOT
QMD
ATOMIC
10⁰
10¹
10²
Plasma temperature T (eV)
Plasma temperature T (eV)
TC13463J1

FIG. 12.

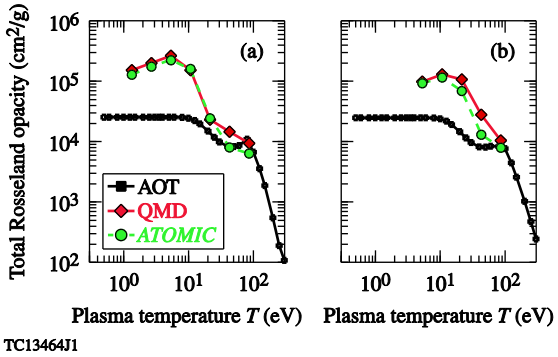
Total Rosseland opacity (cm²/g)
10⁶
10⁵
10⁴
10³
10²
(a)
(b)
AOT
QMD
ATOMIC
10⁰
10¹
10²
Plasma temperature T (eV)
Plasma temperature T (eV)
TC13464J1

FIG. 13.

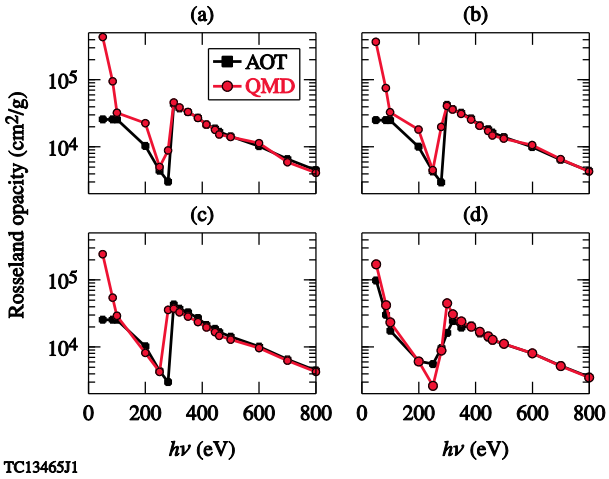
(a)
(b)
(c)
(d)
AOT
QMD
Rosseland opacity (cm²/g)
10⁵
10⁴
0
200
400
600
800
hν (eV)
TC13465J1

FIG. 14.

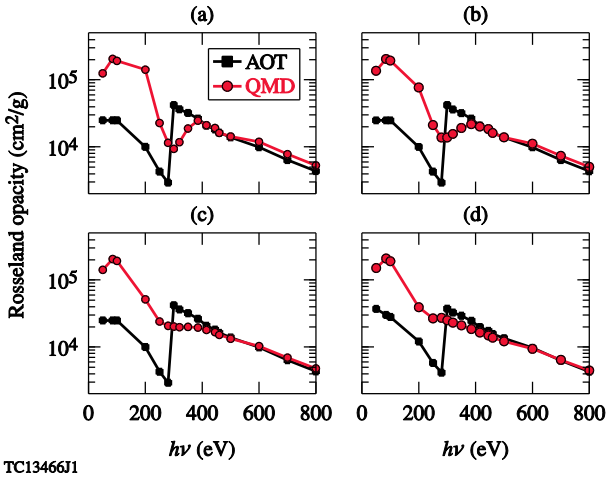
(a)
(b)
(c)
(d)
AOT
QMD
Rosseland opacity (cm²/g)
10⁵
10⁴
0
200
400
600
800
hν (eV)
TC13466J1